ACS APPLIED MATERIALS & INTERFACES

www.acsami.org

Research Article

Electrochemically Active In Situ Crystalline Lithium-Organic Thin Films by ALD/MLD

Jenna Multia,[†] Juho Heiska,[†] Aida Khayyami, and Maarit Karppinen*

Cite This: *ACS Appl. Mater. Interfaces* 2020, 12, 41557–41566

Read Online

ACCESS | Metrics & More | Article Recommendations | Supporting Information

ABSTRACT: Intercalated metal–organic framework (iMOF) type electrochemically active aromatic metal carboxylates are intriguing material candidates for various energy storage devices and microelectronics. In this work, we grow in situ crystalline thin films of such materials through atomic/molecular layer deposition (ALD/MLD); the remarkable benefit of this approach is the possibility to evaluate their electrochemical properties in a simple cell configuration without any additives. Five organic linkers are investigated in combination with lithium: terephthalic acid (TPA), 3,5-pyridinedicarboxylic acid (PDC), 2,6-naphthalenedicarboxylic acid (NDC), 4,4′-biphenyldicarboxylic acid (BPDC), and 4,4′-azobenzenedicarboxylic acid (AZO). In particular, the electrochemical activity of Li-PDC and the crystal structure of Li-AZO are addressed here for the first time. We believe that the in situ gas-phase thin-film deposition is a crucial requirement to benefit from the iMOF-type electrode materials in, e.g., microelectronics and wearable devices.

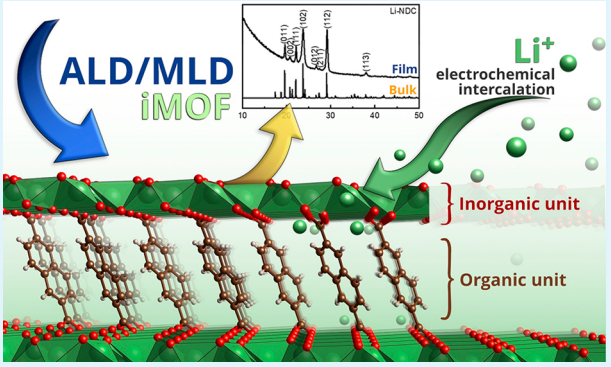

KEYWORDS: *atomic layer deposition, molecular layer deposition, thin film, metal–organic framework, energy storage, organic electrode*

INTRODUCTION

Certain metal–organic compounds, sometimes referred to as intercalated metal–organic frameworks (iMOFs), possess the extremely attractive attribute of experiencing only minimal changes in crystal structure upon (electrochemical) metal ion intercalation/deintercalation.[1−6] Such materials could provide us novel solutions to overcome one of the notorious drawbacks of conventional metal oxide electrode materials in Li-ion battery technology, that is, the capacity decay on cycling due to the substantial volume changes during the Li^+-ion intercalation.[7,8] Another attractive feature of the iMOF structures is that they are not ion specific but could be—besides the Li^+ ions—utilized in next-generation battery technologies based on, e.g., Na^+ ions.[9] An iMOF could be defined as (i) a layer-structured inorganic–organic material, in which (ii) the intercalated metal ions in the inorganic layer originate from the redox-active organic moiety and which is (iii) highly robust against structural changes upon this metal-ion intercalation.[3]

The metal-ion (de)intercalation in iMOFs is dominated by a flexible organic moiety.[1] This scheme is significantly different from the conventional inorganic electrode materials in which there is a rigid lattice site for the moving metal ions, making them very ion specific. The Li^+-ion storage mechanism of iMOFs has been studied in detail for aromatic π-conjugated carbonyls; the Li-oxide layer provides both the transport pathway and storage site for ions, while the organic layer acts as the electron transport pathway and the redox center.[10,11]

Owing to their peculiar electrochemical properties, iMOF-like materials are intriguing electrode candidates for various energy storage devices.[1,10−12] Moreover, thanks to their organic components, they are mechanically flexible and thus particularly appealing, e.g., for wearable electronics.[13] Also, these materials could be used as hybrid capacitors, since their potential lies within the desired range, making them safer than graphite (no dendrites) and better than, e.g., lithium titanate regarding the power density. In addition, it has been shown that lithium 2,6-naphthalenedicarboxylate (Li-NDC) and lithium 4,4′-biphenyldicarboxylate (Li-PBDC) become electronically conductive in their fully lithiated state (with a built-in thermal shut-down mechanism), which could open up a plethora of other applications, e.g., organic transistors.[2,14]

In Figure 1, well-established examples of electrochemically active Li-based iMOFs are shown, for which the "zero-volume-change condition" upon a full electrochemical charge/discharge cycle has been demonstrated; these include—besides the aforementioned Li-NDC[3] and Li-BPDC[2] compounds—lithium terephthalate (Li-TPA).[15] Pyridinedicarboxylate

Received: June 29, 2020
Accepted: August 20, 2020
Published: August 20, 2020

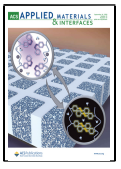

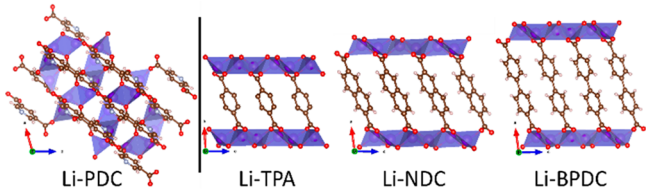

Figure 1. Visualization of Li-PDC,[20] Li-TPA,[47] Li-NDC,[4] and Li-BPDC[21] structures using VESTA.[70]

(PDC) structures are also interesting candidates for iMOF materials; indeed, for some of them, electrochemical activity has already been reported, e.g., Li-2,6-PDC,[16] Na-2,5-PDC,[17] Mn-3,5-PDC,[18] and Zn-2,5-PDC.[19] Considering the possible Li-based iMOF candidates, for lithium 3,5-pyridinedicarboxylic acid (referred to as Li-PDC in the following), the crystal structure is known,[20] but the electrochemical performance has not been investigated.

The iMOF materials are exceptionally lightweight, which is also reflected in the names of their structures, i.e., ULMOF[4] (UL = ultralight). For example, the structures of Li-NDC, Li-BPDC, and Li-PDC are known as ULMOF-1,[4] ULMOF-2,[21] and ULMOF-4,[20] respectively. Among these, the ULMOF-1 and ULMOF-2 structures are isoreticular, while the ULMOF-4 structure of Li-PDC is different in the sense that there are multiple coordination sites (N and O acceptors) which can participate in metal bonding in a multidentate fashion.[20]

From the redox standpoint, Li-TPA, Li-NDC, and Li-PBDC behave similarly, the only difference being in their redox potentials.[2,3,15] By increasing the size of the conjugated organic backbone, the LUMO of the carbonyl group can be lowered, the redox potential decreased, and the structural stability increased against the metal-ion intercalation.[22] However, the larger organic backbone also leads to lower volumetric/gravimetric capacity.[9]

In order to truly benefit from the iMOF materials in, e.g., microelectronics and wearable devices, development of industry-feasible solvent-free thin-film fabrication techniques with precise thickness control and a possibility to deposit the film over various 3D surface architectures would be necessary. The strongly emerging atomic/molecular layer deposition (ALD/MLD) thin-film technique[23−25] provides us with unique advantages. Like its parent commercially well-established ALD technology, the combined ALD/MLD technique for hybrid inorganic−organics is based on self-limiting gas-surface reactions of alternatingly pulsed gaseous precursors. This enables the large-area uniformity and precise thickness control of the resultant thin films. Using the industry-feasible ALD/MLD technique could be an important step along the roadmap toward devices based on new exciting metal−organic materials for, e.g., microelectronics and sensing applications.[26,27]

So far, new ALD/MLD processes have been developed for tens of amorphous and crystalline inorganic−organic materials, both previously known and completely new.[28−36] In particular, we recently fabricated a series of crystalline s-block-metal-based TPA and PDC thin films through ALD/MLD.[28,30,33,34,37] Here in this work, we investigate the ALD/MLD growth, structures, and electrochemical activity of five different lithium dicarboxylate (iMOF) materials; see Figure 2 for the molecular structures of their organic components. Prior to the present work, ALD/MLD processes were already known for Li-TPA and Li-PDC, while for Li-NDC, Li-BPDC, and Li-AZO new processes were first developed. Recently, Lausund et al.[38] utilized the NDC and BPDC precursors in combination with $ZrCl_4$ (followed by post-deposition acid treatment) to prepare crystalline thin films with a known MOF phase. The NDC precursor has also been used earlier with zinc acetate to yield IRMOF-8 films after a post-deposition treatment with dimethylformamide.[39] As for the AZO precursor, we recently employed it for the deposition of amorphous Zn-AZO[40] and crystalline Fe-AZO[41] films. It should also be noted that bulk samples of Li-AZO were recently synthesized through solvothermal synthesis, but the crystal structure was not reported.[42] Nevertheless, the material showed very promising electrochemical performance; during the electrochemical cycling, the N=N bond is apparently cleaved, making the mechanism very different from those of other carboxylates.

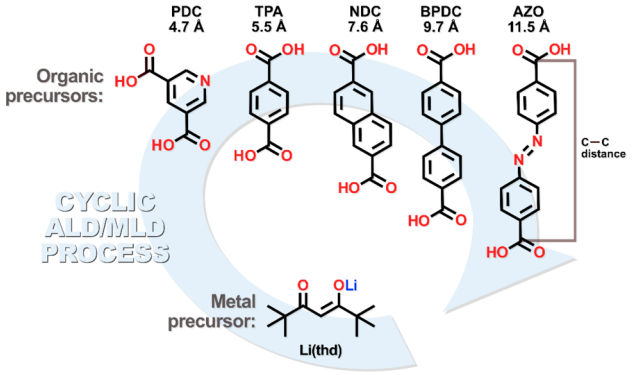

Figure 2. Precursors and the concept of our ALD/MLD processes. The indicated length between the two carbonyl carbons is approximated using Chem3D with MM2 force field energy minimized precursor molecules.

MATERIALS AND METHODS

Thin-Film Deposition. In our ALD/MLD processes, we employed Li(thd) complex (thd = 2,2,6,6-tetramethyl-3,5-heptanedione; synthesized in-house) as the metal precursor and terephthalic acid (TPA; Tokyo Chemical Industry Co., Ltd., >99.0% purity), 3,5-pyridinedicarboxylic acid (PDC; Tokyo Chemical Industry Co., Ltd., 98.0% purity), 2,6-naphthalenedicarboxylic acid (NDC; Tokyo Chemical Industry Co., Ltd., >98.0% purity), 4,4′-biphenydicarboxylic acid (BPDC; Tokyo Chemical Industry Co., Ltd., >97.0% purity), and 4,4′-azobenzenedicarboxylic acid (AZO; Tokyo Chemical Industry Co., 95% purity) as the organic precursors. The depositions were carried out in a commercial flow-type hot-wall ALD reactor (F-120 by ASM Microchemistry Ltd.); for the details of the reactor configuration, see the Supporting Information (Figure S8). The solid precursors were kept in open glass crucibles inside the reactor. The reactor pressure was ∼3 mbar, and nitrogen (99.999%; Parker HPN 5000 N_2 generator) was used as both the purging and carrier gas.

The thin films were deposited on Si(100) substrates (3.0 × 3.0 cm^2) at different temperatures in the range 210−300 °C. Table 1 summarizes the sublimation temperatures and final deposition temperatures chosen for each ALD/MLD process. Sublimation temperatures were derived from our thermal analysis of the organic precursor samples.[43] These thermogravimetric measurements were run on a modified PerkinElmer TGA 7 thermobalance under a flowing nitrogen atmosphere at a low pressure of ca. 4 mbar. In a typical experiment, a sample of 5−10 mg was heated with a rate of 2 °C/min; the section area of the crucible was 0.181 cm^2.

Characterization. The crystallinity/crystal structure was confirmed for the films using grazing incidence X-ray diffraction (GIXRD; X'Pert Pro, PANalytical; Cu Kα) measurements. The film thickness and density were determined through X-ray reflectivity (XRR) measurements using the same equipment. In the measurements, the

https://dx.doi.org/10.1021/acsami.0c11822
ACS Appl. Mater. Interfaces 2020, 12, 41557−41566

Table 1. Precursor Sublimation Temperatures (Chosen Based on Thermogravimetric Analysis in a N_2 Vacuum), Pulse/Purge Lengths, and Deposition Temperatures Used

precursor	$T_{dep.}$ (°C)	$T_{subl.}$ (°C)	TG (°C)	pulse/purge lengths (s)
Li(thd)		174		4/4
TPA	220	185	236	10/30
PDC	220	190	210	15/30
NDC	220	220	275	10/20
BPDC	240	240	289	20/30
AZO	270	250	325	20/30

time per step was set at 20 and 6 s in GIXRD and XRR, respectively, and in the GIXRD measurements, an incidence angle of 0.5° was used. The film thickness values were determined from the averages of the values calculated using the direct calculation and the Fourier methods. For the thickest films (>100 nm), the thicknesses were determined with spectroscopic ellipsometer measurements by a Woollam Spectroscopic Ellipsometer using CompleteEASE software for data analysis. The density of the films was deduced from the critical angle θ_c in the XRR patterns, as follows: $\rho_e = (\theta_c^2\pi)/(\lambda^2 r_e)$, where ρ_e is the mean electron density, λ is the X-ray wavelength, and r_e is the classical electron radius. By assuming the elemental composition being that of pure lithium-dicarboxylate, the mass density was estimated from $\rho_m = (\rho_e A)/(N_A Z)$, where A is the average molar mass, N_A is the Avogadro constant, and Z is the average atomic number. GIXRD of the Li-AZO was compared to other structures, and it was assumed to share a space group with other dicarboxylates. Four peak positions (100), (110), (111), and (112) were chosen to calculate the lattice parameters of Li-AZO using the *d*-spacing formula for a monoclinic lattice. The interaxial angle was estimated to be similar to Li-BPDC.

Chemical composition/bonding was studied by Fourier transform infrared (FTIR) spectroscopy. The measurements were carried out in transmission mode with a Bruker alpha II instrument in the range 400−4000 cm^{-1} using a resolution of 4 cm^{-1} and analyzed from 24 measured spectra. A spectrum of blank Si was subtracted from the spectra to compensate for the effect of the substrate. Scanning electron microscope (SEM) images were recorded with a Tescan Mira 3 FEG-SEM instrument using an in-beam detector and secondary electrons with a 10 kV accelerating voltage. The samples were coated with 8:2 Au/Pd prior to imaging.

Electrochemical characterizations were carried out for thin films deposited on stainless steel substrates (Ø 15.5 mm). The film thickness could not be measured from the steel substrate, and therefore, we chose to only show the areal capacity of the electrodes and focus on the intrinsic properties of the electrodes. The electrode thickness was chosen to be ca. 110 nm, approximated from the growth behavior on a silicon wafer. Before transferring the samples into the glovebox (<1 ppm of oxygen and <0.1 ppm of H_2O), they were dried overnight at 110 °C in a vacuum oven. The thin-film electrodes were assembled in a glovebox and directly applied as electrodes in a CR2016 coin cell with a lithium metal counter electrode. The electrolyte was 1 M $LiPF_6$ in 1:1 EC:DMC. The cells were left to stabilize for 24 h before measurements. The galvanostatic cycling was conducted in a Neware battery testing unit with various current densities. Cyclic voltammetry (CV) was carried out on an Autolab potentiostat (PGSTAT302N) using Nova software with scan rates of 0.1, 0.5, 1.0, and 5.0 mV. Before the scan, the potential was swept to 2.0 V, which was used as a starting point for CV.

RESULTS AND DISCUSSION

ALD/MLD Process Development. Among the five Li-based iMOF materials targeted in this work, ALD/MLD processes were already developed in earlier works for Li-TPA and Li-PDC; then, among the newly developed processes for Li-NDC, Li-BPDC, and Li-AZO materials, the first one was most thoroughly investigated. In the following, we summarize these process optimization results for the Li-NDC films as an exemplary case.

First, we investigated the growth-per-cycle (GPC) values as a function of the precursor pulse lengths for Li-NDC films; for these experiments, the deposition temperature was fixed to 220 °C (for others, see Table 1) and the number of ALD/MLD cycles to 150. The GPC values were calculated from the XRR-determined film thickness values; an example of a typical XRR curve is shown in the inset of Figure 3c. From Figure 3b, it can be seen that the GPC value is saturated when the Li(thd) pulse length is 4 s (N_2 purge 4 s) and the NDC pulse length is 10 s (N_2 purge 20 s). These values are in line with those previously observed for Li-TPA and Li-PDC.[24,29,33,37] Next, we investigated the growth rate at different temperatures (Figure 3a), to find out that the GPC decreases with increasing deposition temperature, which is a common but poorly understood feature in ALD/MLD.[33,44,45] The organics employed have very low vapor pressures in addition to their bifunctionality, which makes them sticky, possibly causing some molecules to stick on the film and act as an extra surface site especially in the lower temperature regime.[46] Nevertheless, even if this is the case, our Li-NDC process can be controlled in an essentially ideal manner as the GPC value saturates over the precursor pulsing time. Finally, the expected fact that the film thickness increases with the number of ALD/MLD cycles applied can be verified from Figure 3c; note that for the films thicker than 50 nm the thickness was measured with a

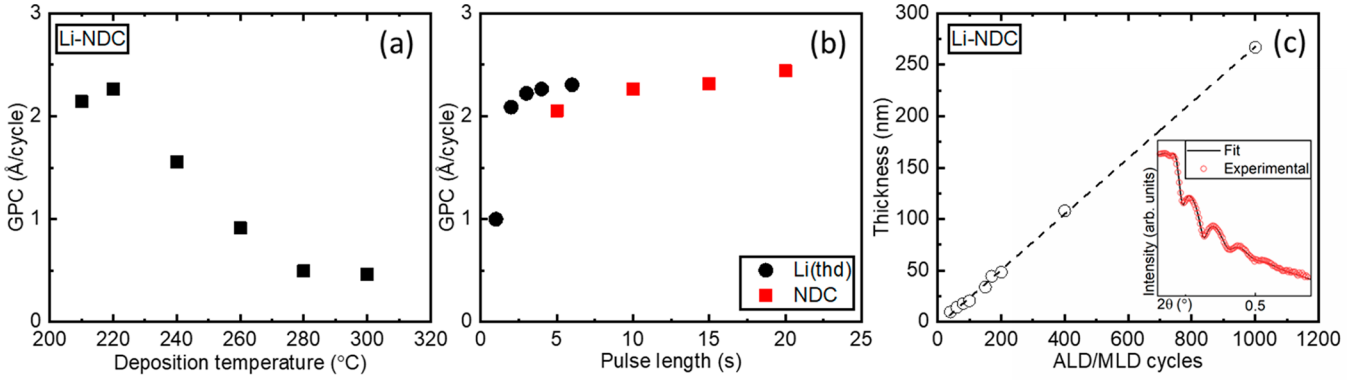

Figure 3. GPC values for the Li-NDC process as a function of (a) deposition temperature and (b) precursor pulse lengths. (c) Thickness of the films as a function of the number of ALD/MLD cycles; the inset shows a representative XRR pattern and its fitting; the number of ALD/MLD cycles is 150 in parts a and b and the inset of part c; the Li(thd)/NDC precursor pulse lengths are 4 s/10 s in parts a and c.

https://dx.doi.org/10.1021/acsami.0c11822
ACS Appl. Mater. Interfaces 2020, 12, 41557−41566

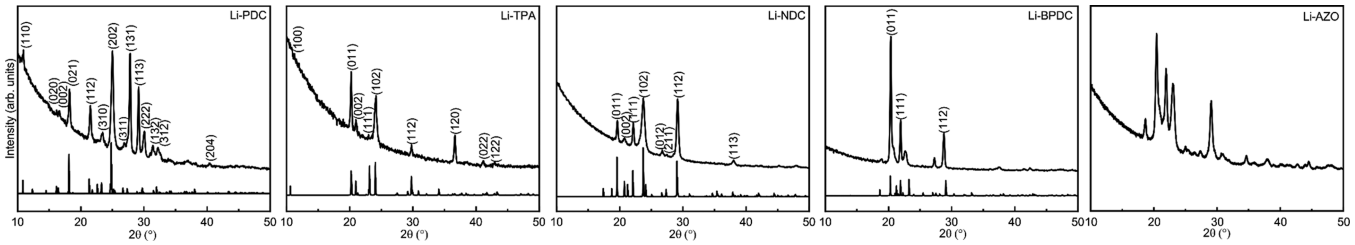

Figure 4. GIXRD patterns for Li-PDC, Li-TPA, Li-NDC, Li-BPDC, and Li-AZO films. The calculated patterns below the measured ones were produced from the reported crystal structures[4,20,21,47] using VESTA[70] software; the experimental patterns were indexed accordingly. For Li-AZO, no previous structure determination data exist, but visual comparison of our GIXRD pattern with the XRD pattern published for a bulk Li-AZO sample (Figure S6a in ref 42) revealed similar peaks (with similar intensity ratios), e.g., at 2θ values of 19, 20, 22, 23, and 29°.

Table 2. Density Values Determined from XRR Data for Our Thin-Film Samples in Comparison to Crystal Structures (and Ideal Densities Calculated from the Crystal Structure Data) Reported in the Literature for Bulk Samples[a]

compound/structure	space group	a (Å)	b (Å)	c (Å)	β (deg.)	V (Å^3)	ideal density (g/cm^3)	exp. density (g/cm^3)	org. backbone length (Å)
Li-PDC $Li_2C_7H_3O_4N$ (ULMOF-4)	$C2/c$[20]	12.69	10.98	11.20	105.8	1501.2	1.58	1.4	5.2
Li-TPA $Li_2C_8H_4O_4$	$P2_1/c$[47]	8.36	5.13	8.48	93.15	363.5	1.63	1.4	6.8
Li-NDC $Li_2C_{12}H_6O_4$ (ULMOF-1)	$P2_1/c$[4]	10.30	5.35	8.66	98.66	471.6	1.61	1.5	8.9
Li-BPDC $Li_2C_{14}H_8O_4$ (ULMOF-2)	$P2_1/c$[21]	12.76	5.14	8.00	97.23	520.6	1.54	1.5	11.0
Li-AZO $Li_2C_{14}H_8O_4N$	$P2_1/c$ (assum.)	14.3 (estim.)	5.0 (estim.)	8.4 (estim.)	97 (assum.)	599	1.56 (estim.)	1.4	12.8

[a]Structural parameters for known bulk structures and calculated Li-AZO structure parameters estimated from the parameters of similar compounds.

spectroscopic ellipsometer and for the rest with both XRR and a spectroscopic ellipsometer.

Parallel process optimizations (similar to those described above) yielded the optimized GPC values for the five processes as follows (in Å/cycle): Li-PDC 2.5,[37] Li-TPA 3.0,[30] Li-NDC 2.3, Li-BPDC 7.0, and Li-AZO 7.0. These values are comparable to those reported for processes with the same organic precursors, i.e., Zr-NDC (8 Å/cycle),[38] Zn-NDC (4.0−4.9 Å/cycle),[39] and Zr-BPDC (10−12 Å/cycle).[38] Particularly interesting is to note that our Li-AZO process yielding crystalline films has a higher GPC (7.0 Å/cycle) compared to that earlier seen for amorphous Zn-AZO (3.0 Å/cycle)[40] films but lower compared to the case of the crystalline Fe-AZO (25 Å/cycle)[41] films. Apparently, the choice of the metal precursor also plays a role, as the more bulky ligands would yield lower surface site densities, allowing the bulky organic molecules to more easily get to the surface, even though this could lead to slower growth rates.[38]

All of our Li(thd)+dicarboxylate processes were found to yield highly crystalline and air-stable thin films for which the GIXRD patterns could be readily indexed—in cases when relevant—according to the structures previously reported for the same materials in bulk samples. In Figure 4, we plot the GIXRD patterns for our Li-PDC, Li-TPA, Li-NDC, Li-BPDC, and Li-AZO films. Three of the structures (Li-TPA, Li-NDC, and Li-BPDC) have the same space group $P2_1/c$, and in the corresponding bulk samples, the b-axis ranges between 5.13 and 5.35 Å and the c-axis between 8.00 and 8.66 Å. The Li-NDC and Li-BPDC structures consist of antifluorite-type layers of corner- and edge-sharing LiO_4 tetrahedra connected by the 2,6-NDC or 4,4′-BPDC linkers to form a 3-D framework, where $\pi-\pi$ interactions between the naphthalene or biphenyl herringbone stacked rings exist.[4,21] Li-TPA forms a similar layered structure with tetrahedrally coordinated lithium cations and the packing of the terephthalate in the herringbone way.[47] The a-axis is varying and is correlated with the length of the organic backbone between the LiO layers (Figure 2, Table 2). To address the structure of Li-AZO (not known from previous works on bulk samples), we assumed the same monoclinic $P2_1/c$ space group as for Li-TPA, Li-NDC, and Li-BPDC and indexed the major peaks accordingly based on the similarities in the GIXRD patterns (Figure 5). Then, we calculated the lattice parameters from the (100), (110), (111), and (112) peak positions (assuming β = 97°) at a = 14.3 Å, b =

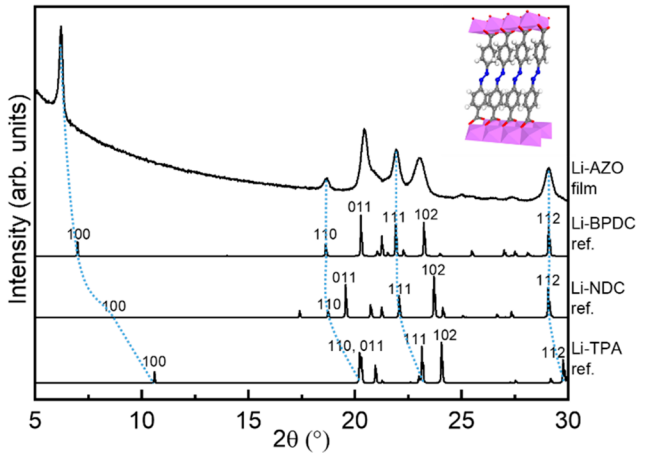

Figure 5. GIXRD pattern for our Li-AZO film, compared to XRD patterns calculated for Li-TPA,[47] Li-NDC,[4] and Li-BPDC[21] based on structure data for bulk samples; peaks connected by blue lines were used in lattice parameter estimation for Li-AZO.

https://dx.doi.org/10.1021/acsami.0c11822
ACS Appl. Mater. Interfaces 2020, 12, 41557−41566

5.0 Å, and c = 8.4 Å; these values reflect well the trend expected based on the organic backbone lengths (Table 2). Moreover, we give in Table 2 both the ideal density values calculated from the crystal structure data and the experimental values determined from the XRR data; it can be seen that the experimental values for our thin films are systematically slightly lower than the ideal values.

The morphology of the samples was investigated with SEM (Figure S1). The polycrystalline nature of the films is evident from the images and the overall appearance of the Li-TPA, Li-NDC, Li-BPDC, and Li-PDC films is very similar, although slight differences in the shape and arrangement of the crystallites are seen; Li-AZO in particular deviates from the rest of the samples, as it clearly consists of smaller crystallites which grow and merge with the film growth. A similar trend is visible in the crystallite size, such that for Li-AZO significantly smaller crystallites were seen compared to the other films (Supporting Information).

In Figure 6, we display the FTIR spectra for the films. First, the spectral range around 3400 cm^{-1} is free from any features

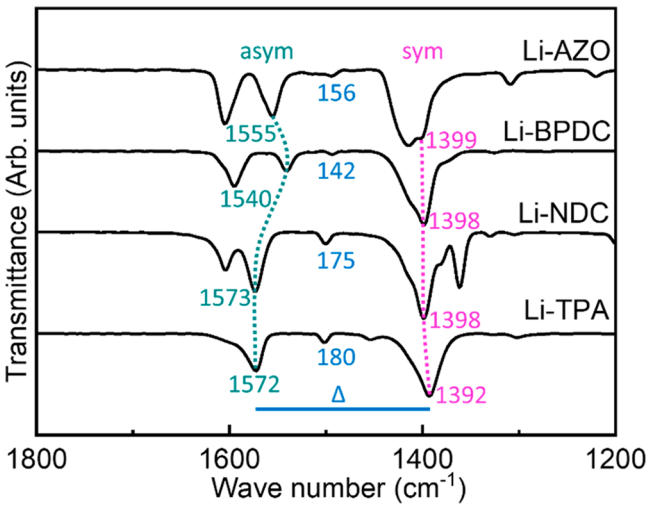

Figure 6. FTIR spectra for Li-TPA, Li-NDC, Li-BPDC, and Li-AZO films: asymmetric and symmetric stretching modes of the carboxylate group are highlighted, and the corresponding Δ values are given in cm^{-1}.

related to incorporated water (Figure S4); this is in line with previous knowledge on bulk-synthesized lithium carboxylates; Li-PDC, Li-TPA, Li-NDC, Li-BPDC, and Li-AZO do not absorb water molecules and are stable up to temperatures of 550,[20] 350,[15] 610,[4] 575,[21] and 410 °C,[42] respectively. We also note that for all of our Li-dicarboxylate thin films the region around 1720 cm^{-1} lacks the absorption band due to free COOH groups; this confirms that during the ALD/MLD process the dicarboxylic acid precursor indeed reacts with lithium. The dominant absorption bands are seen in all of the spectra around 1400 and 1600 cm^{-1}, arising from the asymmetric and symmetric stretch of the carboxylate group, respectively. The visibly sharp COO^- bands seen are consistent with the crystalline nature of these films. Most importantly, the distance (Δ) between the two carboxylate absorption bands (Figure 6) provides us strong support toward the bidentate bridging-type bonding mode in our Li-dicarboxylate thin films, which is expected for 130 cm^{-1} < Δ < 200 cm^{-1}.[48,49] Note that the FTIR spectrum for Li-PDC was discussed in detail in our previous work[37] and thus left out from the present discussion. Nevertheless, it should be mentioned that the spectrum confirmed the participation of the pyridyl-N entity in the metal coordination. It should also be mentioned that the other absorption bands seen in Figure 6 around 1400−1600 cm^{-1} are aromatic backbone vibrations.[50−53] In the solid state, the vibrations are often coupled, meaning that one single peak is often a sum of many different fundamental vibrations. For example, for Li-NDC, the COO^- asymmetric stretch is probably coupled with the skeletal vibration of the naphthalene backbone. The listed peak positions are based on the assumption that the given peak is mainly caused by the given fundamental vibration.[54] Finally, we note that the FTIR spectrum for our Li-AZO film is very similar to the spectrum reported in the literature for a bulk sample.[42]

Electrochemical Performance. From Figure 7, it is clear that all of our iMOF thin-film electrodes are electroactive. In previous studies, the electrochemical performance of bulk samples has been reported for other materials except for Li-PDC.[2,3,15,42] Here, in this work, our main goal is to assess the material performance in thin-film form—not necessarily even expecting similar performance as in the bulk. The intriguing fact is that our thin-film electrodes do not contain any additives such as conductive carbon or binder. Therefore, the electrochemical performances measured here can be taken to better reflect the intrinsic properties of the iMOF materials themselves and their basic interactions with the electrolyte. To guarantee similar conditions for, e.g., Li^+-ion diffusion and electron conductivity and thereby enable better comparison among our different Li-dicarboxylate samples, we fixed the thickness of our thin-film electrodes to 110 nm.

CVs with different scan rates (Figure S2) show the electrochemical activity of these materials. Clear lithiation of the materials is seen for Li-TPA (0.81 V), Li-NDC (0.73 V), Li-BPDC (0.66 V), and Li-AZO (1.48 V), matching well with the previously reported values.[6,15,22,42] Li-PDC does not show any clear redox peaks but a more capacitor-like behavior. The electrochemical behavior of para-positioned pyridine dicarboxylates is well characterized (showing a plateau caused by carboxylate),[17] but the meta-positioned dicarboxylates still lack in-depth studies.[16,18]

Galvanostatic cycling started with a rate capability test followed by a longer cycling period (Figure 7). The different current densities used are shown therein. In addition, the (dis)charge curves from selected cycles are shown in Figure 8 to highlight the differences and few observations occurring during cycling.[54] As in the half-cell, these materials are applied vs Li^+/Li and they actually function as positive electrodes (cathodes) and therefore are lithiated during discharge.

The large irreversible capacity during the first cycle is attributed to the formation of a solid electrolyte interphase (SEI).[53] The capacity retention during rate capability tests from 1.1 to 53.0 $\mu A/cm^2$ for Li-TPA, Li-NDC, Li-BPDC, Li-AZO, and Li-PDC was ca. 61, 50, 41, 71, and 60%, respectively. After 150 cycles, the materials retained 58, 61, 44, 88, and 87% of their capacity, respectively. When comparing solely the obtained capacity retention values, it is quite clear that Li-TPA performs best out of these Li-dicarboxylates. Previously, Li-NDC and Li-BPDC have been reported to possess better rate capabilities and at least comparable cyclabilities.[22] In our later discussion, we try to

https://dx.doi.org/10.1021/acsami.0c11822
ACS Appl. Mater. Interfaces 2020, 12, 41557−41566

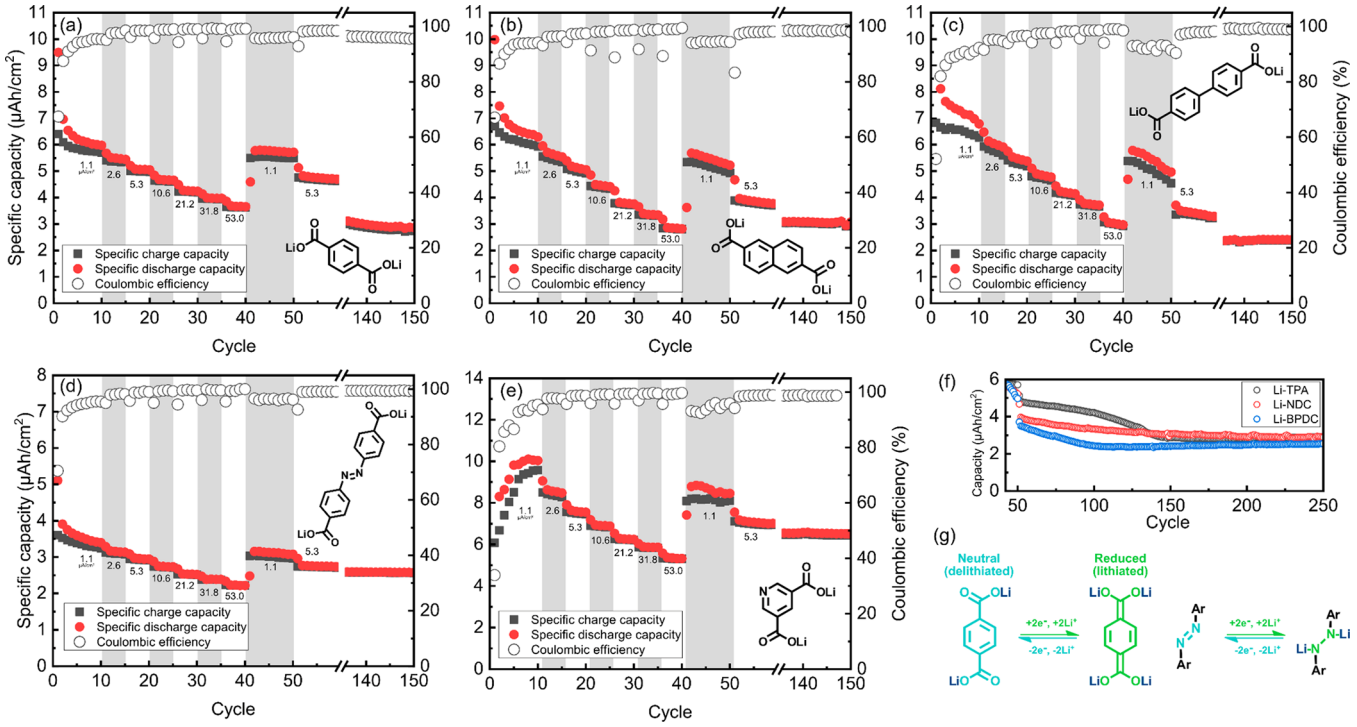

Figure 7. Galvanostatic cycling data with various current densities for (a) Li-TPA, (b) Li-NDC, (c) Li-BPDC, (d) Li-AZO, and (e) Li-PDC. (f) Decreasing capacity of Li-TPA (black), Li-NDC (red), and Li-BPDC (blue) after the current density experiment. (g) Schematic illustration of redox reactions of Li-dicarboxylates, using Li-TPA and Li-AZO as examples.

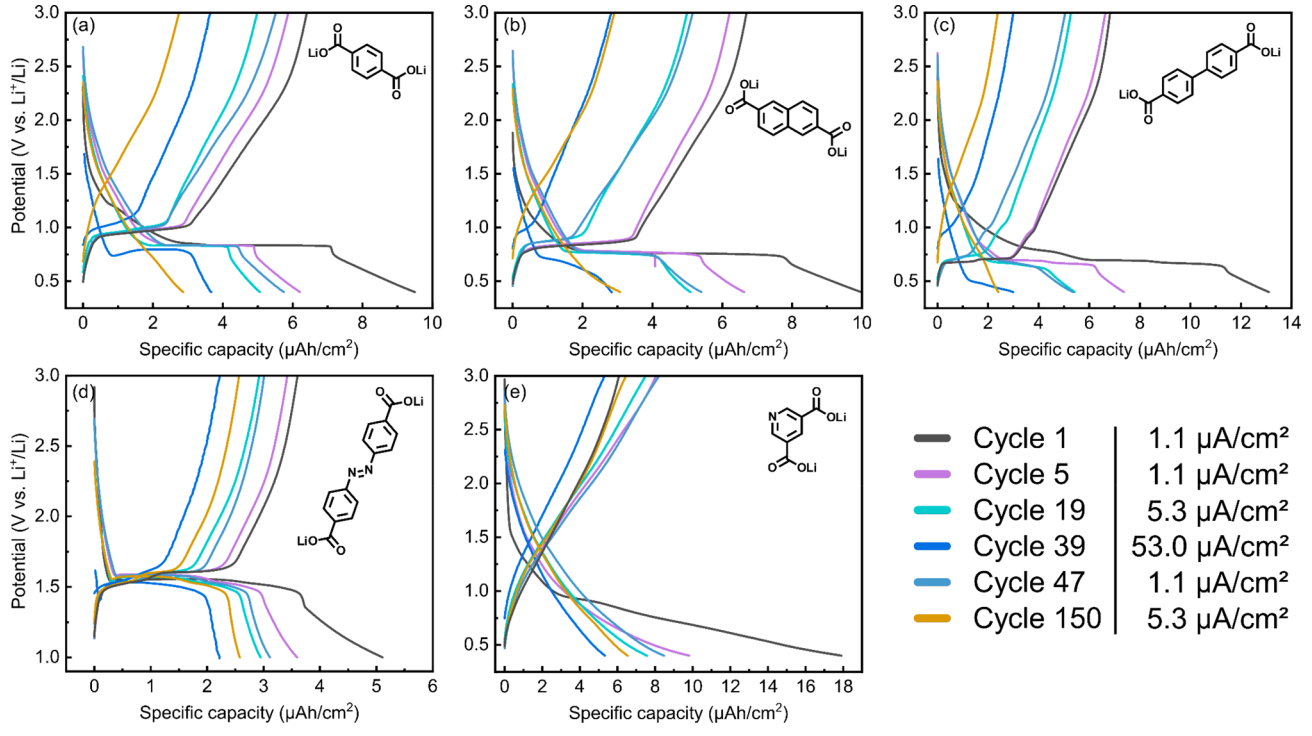

Figure 8. (a–e) Charge–discharge curves of Li-TPA, Li-NDC, Li-BPDC, Li-AZO, and Li-PDC, respectively; color coding and current densities are indicated in the legend.

rationalize the possible reasons for the present observations which partly differ from those reported for bulk samples.

From Figure 7, both Li-AZO and Li-PDC perform very well, although the comparison to other Li-dicarboxylates is not entirely feasible because of the different electrochemical redox mechanisms. Our Li-AZO thin-film sample shows very similar performance to that previously reported for bulk Li-AZO samples,[42] with two plateaus and similar values for redox potential, polarization, and capacity retention. Therefore, it can be concluded that lithium is inserted with the same N═N cleavage mechanism and the material is working in excellent fashion as a thin-film electrode. The Li-PDC thin film also

https://dx.doi.org/10.1021/acsami.0c11822
ACS Appl. Mater. Interfaces 2020, 12, 41557–41566

performs well, but it has a different (sloping) voltage profile after the first cycle. Previous reports of pyridine-type compounds have shown that carboxylates in the para position tend to yield plateaus that resemble those of their terephthalate analogues, although the redox potentials are typically higher.[17,18] On the other hand, the sloping voltage profile is often seen in polymer batteries, where the state of lithiation heavily affects the redox potential. This is an indication of more connected redox units, compared to the isolated carboxylate units, e.g., in terephthalate.[55,56] Thus, further experiments are required to fully verify the redox mechanism of our Li-PDC films and answer the question of whether it involves the carboxylate groups or the pyridine ring.[55,57] Nevertheless, as there is no plateau nor peaks in CV, we tentatively believe that the reaction is not Faradaic in nature.

From Figure 8, the lithiation (discharge) potentials for our Li-TPA, Li-NDC, and Li-BPDC thin films are found to be ca. 0.83, 0.76, and 0.68 V, respectively, well in line with those reported for bulk materials.[2,3,15] The polarization of the plateau also decreases—as expected—with increasing size of the aromatic core, from 0.14 V of Li-TPA to 0.09 V of Li-NDC and further to 0.02 V for Li-BPDC. For Li-TPA and Li-NDC, only one continuous plateau can be distinguished; Li-PBDC shows two (at 0.70 and 0.66 V), in line with the previous reports where the mechanism was confirmed to be step-by-step lithiation of the carbonyls.[22] The sloping part of the (dis)charge curve (ca. 0.7−0.4 V) is possibly caused by the "superlithiation", i.e., lithiation of the aromatic core.[58]

The same voltage profile is retained by the Li-dicarboxylates even with high current densities and at least up to 50 cycles. However, by 150 cycles, all of the carboxylates have lost their typical voltage profiles and have transformed into sloping voltage profiles (Figures 7f and 8). In a previous study by Lee et al.[58] with Li-TPA bulk samples, this was attributed to the lithiation of the aromatic skeleton where the same changes in the voltage profile and increased polarization were observed over extended cycling.[58] We also argued this to be the case with another terephthalate analogue studied in thin-film form, for which we saw the degradation of crystallinity upon extended cycling.[59] As these materials are very similar to the materials studied in this study, this might suggest that the amorphization or gradual degradation of the crystal structure could be a rather common feature of these Li-dicarboxylates when cycled between 3.0 and 0.4 V.

The Coulombic efficiency (CE) of these materials is also behaving rather interestingly. With the low current density, i.e., when the intercalation speed of lithium is slow, the CE for Li-TPA, Li-NDC, and Li-PBDC was found to be ca. 98, 94, and 92%, respectively, while, with high current density, it was 99% for all of our Li-dicarboxylate films. The carbonyl reaction itself should be fast.[60] However, the lithiation reaction of the aromatic skeleton could be considered to be a slow one and kinetically controlled;[60−62] in such a situation when the cell is cycled with higher current density, the slower reaction may not have enough time to occur before the cut-off potential is reached.

A plausible explanation for the low CE with the low current densities could be amorphization/gradual degradation of the structure; the fact that the CE is lowered in particular with the larger organic backbones for which there are more sites for the lithiation of the aromatic skeleton to occur[61,62] further supports this explanation. To study this, we conducted post-mortem GIXRD and ATR-FTIR analyses for the Li-TPA, Li-NDC, and Li-BPDC electrodes (Figures S5−S7). The GIXRD clearly showed that the crystallinity of the materials was degraded upon cycling. The main reflections became almost completely invisible, and in the Li-PBDC case, a new unidentified peak appeared. The ATR-FTIR spectra for the cycled electrodes actually look very similar at a first glance, indicating that the SEI or the degradation product of these materials is very similar. Nevertheless, tiny differences are seen in the 1800−1300 cm^{-1} range, i.e., in the range originating from the asymmetric and symmetric carboxylate vibrations. In the cycled electrodes, there are no shoulders or peaks visible in the exact positions where the asymmetric carboxylate peak lies in the pristine electrode. The asymmetric carboxylate peak is a better indicator of the changes in the structure than the symmetric one, since it is more sensitive to possible changes in the electron and coordination structure.[63] Therefore, we believe that these materials are undergoing changes upon long-term cycling indicated by changes in voltage plateau and the post-mortem analysis.

In previous works, the higher CE values with the larger current densities are sometimes attributed to the slow kinetics of the lithiation or the conductive carbon present in the cell design;[53,54,64,65] however, in our thin-film electrodes, conductive carbon is not present. We also note that the crystal structure could be an important factor to achieve good cyclability and capacity.[66] Fédèle et al.[22] also proposed solvent co-intercalation with the Li^+ ions with Li-BPDC. To address these questions in future studies, choosing narrower potential ranges or minimizing the possible electrolyte co-intercalation or other side reactions, e.g., by coating could be considered.[9,30,61,67−69]

CONCLUSIONS

We have demonstrated that an entire family of in situ crystalline thin films of lithium-based iMOF-type materials can be readily fabricated from gaseous precursors using the ALD/MLD technique. In our comparative study, we combined the lithium precursor Li(thd) with five different organic precursors: TPA (terephthalic acid), PDC (3,5-pyridinedicarboxylic acid), NDC (2,6-naphthalenedicarboxylic acid), BPDC (4,4′-biphenyldicarboxylic acid), and AZO (4,4′-azobenzenedicarboxylic acid). The deposition processes carried out at 220−270 °C yielded high-quality air-stable thin films at the appreciably high growth rate ranging from 2.3 to 7.0 Å/cycle.

For four of the Li-dicarboxylate thin-film materials studied (Li-TPA, Li-PDC, Li-NDC, Li-BPDC), crystal structures could be assigned based on their GIXRD and FTIR data to those previously reported for corresponding bulk samples. For Li-AZO, based on the close resemblance of the GIXRD and FTIR data, we assumed the same monoclinic $P2_1/c$ space group as that for Li-TPA, Li-NDC, and Li-BPDC and indexed the major diffraction peaks accordingly to corroborate the monoclinic symmetry and estimate the unit cell parameters. We also determined the densities for all five thin films based on XRR data, to confirm that they were in line (systematically slightly lower) than the ideal density values calculated from the crystal structures.

Galvanostatic cycling experiments verified the electrochemical activity expected for an iMOF, i.e., lithium (de)intercalation, for all five of the Li-dicarboxylates investigated, notably, for the first time in the case of Li-PDC. Also importantly, our approach (gas-phase electrode fabrication without additives and parallel experimental procedures for all

https://dx.doi.org/10.1021/acsami.0c11822
ACS Appl. Mater. Interfaces 2020, 12, 41557−41566

samples) allowed us—for the first time—to address the intrinsic electrochemical characteristics of the different iMOF materials in a comparative manner. With this comparison, we managed to shed light on the possible degradation mechanism of the Li-dicarboxylates, which is still poorly understood but vital information for the actual applicability of these materials.

The iMOF-type electrode materials possess a number of superior chemical features over the traditional transition metal oxide electrode materials. We thus believe that our work will boost the research on these materials as intriguing new components for various energy storage devices, in particular in applications requiring the electrode materials in high-quality flexible thin-film form. Moreover, we would like to emphasize that our approach is not limited only to the Li-based carboxylates taken as a model case here.

■ ASSOCIATED CONTENT

Supporting Information

The Supporting Information is available free of charge at https://pubs.acs.org/doi/10.1021/acsami.0c11822.

Figure S1, SEM image of the films; Figure S2, voltammograms of the films; Figure S3, thermogravimetric analysis graphs of the organic precursors; Figure S4, full FTIR spectra of the films; Figures S5−S7, post-mortem analysis of the electrodes; Figure S8, schematic of the ALD reactor; Table S1, FWHM values of the thin films; Scherrer equation for determining crystallite size and appropriate data (PDF)

■ AUTHOR INFORMATION

Corresponding Author

Maarit Karppinen − *Department of Chemistry and Materials Science, Aalto University, FI-00076 Aalto, Finland;* orcid.org/0000-0003-1091-1169; Email: maarit.karppinen@aalto.fi

Authors

Jenna Multia − *Department of Chemistry and Materials Science, Aalto University, FI-00076 Aalto, Finland*

Juho Heiska − *Department of Chemistry and Materials Science, Aalto University, FI-00076 Aalto, Finland*

Aida Khayyami − *Department of Chemistry and Materials Science, Aalto University, FI-00076 Aalto, Finland*

Complete contact information is available at: https://pubs.acs.org/10.1021/acsami.0c11822

Author Contributions

All authors have given approval to the final version of the manuscript.

Author Contributions

†J.M., J.H.: These authors contributed equally.

Funding

The present work has received funding from the European Research Council under the European Union's Seventh Framework Programme (FP/2007−2013)/ERC Advanced Grant Agreement (No. 339478) and Academy of Finland (No. 296299).

Notes

The authors declare no competing financial interest.

■ ACKNOWLEDGMENTS

This work made use of the RawMatTERS Finland infrastructure (RAMI) and Aalto Nanomicroscopy Center (Aalto NMC) facilities based at Aalto University. Mr. Ramin Ghiyasi is thanked for the Li-AZO structure sketch. Mr. Olli Sorsa is thanked for providing insight on the electrochemical characterization.

■ ABBREVIATIONS

iMOF, intercalated metal−organic framework; ALD/MLD, atomic/molecular layer deposition; UL, ultralight; TPA, terephthalic acid; PDC, 3,5-pyridinedicarboxylic acid; NDC, 2,6-naphthalenedicarboxylic acid; BPDC, 4,4′-biphenyldicarboxylic acid; AZO, 4,4′-azobenzenedicarboxylic acid; GIXRD, grazing incidence X-ray diffraction; XRR, X-ray reflectivity; FTIR, Fourier transform infrared; thd, 2,2,6,6-tetramethyl-3,5-heptanedione.

■ REFERENCES

(1) Li, C.; Hu, X.; Lou, X.; Zhang, L.; Wang, Y.; Amoureux, J.-P.; Shen, M.; Chen, Q.; Hu, B. The Organic-Moiety-Dominated Li + Intercalation/Deintercalation Mechanism of a Cobalt-Based Metal−Organic Framework. *J. Mater. Chem. A* **2016**, *4*, 16245−16251.

(2) Ozawa, Y.; Ogihara, N.; Hasegawa, M.; Hiruta, O.; Ohba, N.; Kishida, Y. Intercalated Metal−Organic Frameworks with High Electronic Conductivity as Negative Electrode Materials for Hybrid Capacitors. *Commun. Chem.* **2018**, *1*, 65.

(3) Ogihara, N.; Yasuda, T.; Kishida, Y.; Ohsuna, T.; Miyamoto, K.; Ohba, N. Organic Dicarboxylate Negative Electrode Materials with Remarkably Small Strain for High-Voltage Bipolar Batteries. *Angew. Chem., Int. Ed.* **2014**, *53*, 11467−11472.

(4) Banerjee, D.; Kim, S. J.; Parise, J. B. Lithium Based Metal-Organic Framework with Exceptional Stability. *Cryst. Growth Des.* **2009**, *9*, 2500−2503.

(5) Yasuda, T.; Ogihara, N. Reformation of Organic Dicarboxylate Electrode Materials for Rechargeable Batteries by Molecular Self-Assembly. *Chem. Commun.* **2014**, *50*, 11565−11567.

(6) Ogihara, N.; Ozawa, Y.; Hiruta, O. A Self-Assembled Intercalated Metal−Organic Framework Electrode with Outstanding Area Capacity for High Volumetric Energy Asymmetric Capacitors. *J. Mater. Chem. A* **2016**, *4*, 3398−3405.

(7) Kim, Y.; Park, K.; Song, S.; Han, J.; Goodenough, J. B. Access to M^{3+}/M^{2+} Redox Couples in Layered $LiMS_2$ Sulfides (M = Ti, V, Cr) as Anodes for Li-Ion Battery. *J. Electrochem. Soc.* **2009**, *156*, A703.

(8) Luo, C.; Zhu, Y.; Xu, Y.; Liu, Y.; Gao, T.; Wang, J.; Wang, C. Graphene Oxide Wrapped Croconic Acid Disodium Salt for Sodium Ion Battery Electrodes. *J. Power Sources* **2014**, *250*, 372−378.

(9) Heiska, J.; Nisula, M.; Karppinen, M. Organic Electrode Materials with Solid-State Battery Technology. *J. Mater. Chem. A* **2019**, *7*, 18735−18758.

(10) Wu, X.; Jin, S.; Zhang, Z.; Jiang, L.; Mu, L.; Hu, Y.-S.; Li, H.; Chen, X.; Armand, M.; Chen, L.; Huang, X. Unraveling the Storage Mechanism in Organic Carbonyl Electrodes for Sodium-Ion Batteries. *Sci. Adv.* **2015**, *1*, e1500330.

(11) Li, C.; Lou, X.; Shen, M.; Hu, X.; Guo, Z.; Wang, Y.; Hu, B.; Chen, Q. High Anodic Performance of Co 1,3,5-Benzenetricarboxylate Coordination Polymers for Li-Ion Battery. *ACS Appl. Mater. Interfaces* **2016**, *8*, 15352−15360.

(12) Poizot, P.; Gaubicher, J.; Renault, S.; Dubois, L.; Liang, Y.; Yao, Y. Opportunities and Challenges for Organic Electrodes in Electrochemical Energy Storage. *Chem. Rev.* **2020**, *120*, 6490−6557.

(13) Wang, C.; Xu, Y.; Fang, Y.; Zhou, M.; Liang, L.; Singh, S.; Zhao, H.; Schober, A.; Lei, Y. Extended π-Conjugated System for Fast-Charge and -Discharge Sodium-Ion Batteries. *J. Am. Chem. Soc.* **2015**, *137*, 3124−3130.

(14) Ogihara, N.; Ohba, N.; Kishida, Y. On/off Switchable Electronic Conduction in Intercalated Metal-Organic Frameworks. *Sci. Adv.* **2017**, *3*, No. e1603103.
(15) Armand, M.; Grugeon, S.; Vezin, H.; Laruelle, S.; Ribière, P.; Poizot, P.; Tarascon, J.-M. Conjugated Dicarboxylate Anodes for Li-Ion Batteries. *Nat. Mater.* **2009**, *8*, 120−125.
(16) Gou, L.; Zhang, H.-X.; Fan, X.-Y.; Li, D.-L. Lithium Based Coordination Polymer as Anode for Li-Ion Battery. *Inorg. Chim. Acta* **2013**, *394*, 10−14.
(17) Padhy, H.; Chen, Y.; Lüder, J.; Gajella, S. R.; Manzhos, S.; Balaya, P. Charge and Discharge Processes and Sodium Storage in Disodium Pyridine-2,5-Dicarboxylate Anode-Insights from Experiments and Theory. *Adv. Energy Mater.* **2018**, *8*, 1701572.
(18) Fei, H.; Liu, X.; Li, Z.; Feng, W. Metal Dicarboxylates: New Anode Materials for Lithium-Ion Batteries with Good Cycling Performance. *Dalt. Trans.* **2015**, *44*, 9909−9914.
(19) Fei, H.; Lin, Y. Zinc Pyridinedicarboxylate Micro-Nanostructures: Promising Anode Materials for Lithium-Ion Batteries with Excellent Cycling Performance. *J. Colloid Interface Sci.* **2016**, *481*, 256−262.
(20) Banerjee, D.; Kim, S. J.; Borkowski, L. A.; Xu, W.; Parise, J. B. Solvothermal Synthesis and Structural Characterization of Ultralight Metal Coordination Networks. *Cryst. Growth Des.* **2010**, *10*, 709−715.
(21) Banerjee, D.; Borkowski, L. A.; Kim, S. J.; Parise, J. B. Synthesis and Structural Characterization of Lithium-Based Metal−Organic Frameworks. *Cryst. Growth Des.* **2009**, *9*, 4922−4926.
(22) Fédèle, L.; Sauvage, F.; Gottis, S.; Davoisne, C.; Salager, E.; Chotard, J.-N.; Becuwe, M. 2D-Layered Lithium Carboxylate Based on Biphenyl Core as Negative Electrode for Organic Lithium-Ion Batteries. *Chem. Mater.* **2017**, *29*, 546−554.
(23) George, S. M. Atomic Layer Deposition: An Overview. *Chem. Rev.* **2010**, *110*, 111−131.
(24) Sundberg, P.; Karppinen, M. Organic and Inorganic−Organic Thin Film Structures by Molecular Layer Deposition: A Review. *Beilstein J. Nanotechnol.* **2014**, *5*, 1104−1136.
(25) Klepper, K. B.; Nilsen, O.; Fjellvåg, H. Deposition of Thin Films of Organic−Inorganic Hybrid Materials Based on Aromatic Carboxylic Acids by Atomic Layer Deposition. *Dalt. Trans.* **2010**, *39*, 11628−11635.
(26) Allendorf, M. D.; Schwartzberg, A.; Stavila, V.; Talin, A. A. A Roadmap to Implementing Metal-Organic Frameworks in Electronic Devices: Challenges and Critical Directions. *Chem. - Eur. J.* **2011**, *17*, 11372−11388.
(27) Lei, J.; Qian, R.; Ling, P.; Cui, L.; Ju, H. Design and Sensing Applications of Metal−Organic Framework Composites. *TrAC, Trends Anal. Chem.* **2014**, *58*, 71−78.
(28) Ahvenniemi, E.; Karppinen, M. Atomic/Molecular Layer Deposition: A Direct Gas-Phase Route to Crystalline Metal−Organic Framework Thin Films. *Chem. Commun.* **2016**, *52*, 1139−1142.
(29) Ahvenniemi, E.; Karppinen, M. In Situ Atomic/Molecular Layer-by-Layer Deposition of Inorganic−Organic Coordination Network Thin Films from Gaseous Precursors. *Chem. Mater.* **2016**, *28*, 6260−6265.
(30) Nisula, M.; Karppinen, M. Atomic/Molecular Layer Deposition of Lithium Terephthalate Thin Films as High Rate Capability Li-Ion Battery Anodes. *Nano Lett.* **2016**, *16*, 1276−1281.
(31) Nisula, M.; Linnera, J.; Karttunen, A. J.; Karppinen, M. Lithium Aryloxide Thin Films with Guest-Induced Structural Transformation by ALD/MLD. *Chem. - Eur. J.* **2017**, *23*, 2988−2992.
(32) Giedraityte, Z.; Lopez-Acevedo, O.; Espinosa Leal, L. A.; Pale, V.; Sainio, J.; Tripathi, T. S.; Karppinen, M. Three-Dimensional Uracil Network with Sodium as a Linker. *J. Phys. Chem. C* **2016**, *120*, 26342−26349.
(33) Penttinen, J.; Nisula, M.; Karppinen, M. Atomic/Molecular Layer Deposition of s-Block Metal Carboxylate Coordination Network Thin Films. *Chem. - Eur. J.* **2017**, *23*, 18225−18231.
(34) Tanskanen, A.; Karppinen, M. Iron-Terephthalate Coordination Network Thin Films Through In-Situ Atomic/Molecular Layer Deposition. *Sci. Rep.* **2018**, *8*, 8976.
(35) Giedraityte, Z.; Sainio, J.; Hagen, D.; Karppinen, M. Luminescent Metal-Nucleobase Network Thin Films by Atomic/Molecular Layer Deposition. *J. Phys. Chem. C* **2017**, *121*, 17538−17545.
(36) Pale, V.; Giedraityte, Z.; Chen, X.; Lopez-Acevedo, O.; Tittonen, I.; Karppinen, M. Excitation-Dependent Fluorescence from Atomic/Molecular Layer Deposited Sodium-Uracil Thin Films. *Sci. Rep.* **2017**, *7*, 6982.
(37) Penttinen, J.; Nisula, M.; Karppinen, M. New S-Block Metal Pyridinedicarboxylate Network Structures through Gas-Phase Thin-Film Synthesis. *Chem. - Eur. J.* **2019**, *25*, 11466−11473.
(38) Lausund, K. B.; Olsen, M. S.; Hansen, P.-A.; Valen, H.; Nilsen, O. MOF Thin Films with Bi-Aromatic Linkers Grown by Molecular Layer Deposition. *J. Mater. Chem. A* **2020**, *8*, 2539−2548.
(39) Salmi, L. D.; Heikkilä, M. J.; Vehkamäki, M.; Puukilainen, E.; Ritala, M.; Sajavaara, T. Studies on Atomic Layer Deposition of IRMOF-8 Thin Films. *J. Vac. Sci. Technol., A* **2015**, *33*, No. 01A121.
(40) Khayyami, A.; Karppinen, M. Reversible Photoswitching Function in Atomic/Molecular-Layer-Deposited ZnO:Azobenzene Superlattice Thin Films. *Chem. Mater.* **2018**, *30*, 5904−5911.
(41) Khayyami, A.; Philip, A.; Karppinen, M. Atomic/Molecular Layer Deposited Iron−Azobenzene Framework Thin Films for Stimuli-Induced Gas Molecule Capture/Release. *Angew. Chem., Int. Ed.* **2019**, *58*, 13400−13404.
(42) Luo, C.; Borodin, O.; Ji, X.; Hou, S.; Gaskell, K. J.; Fan, X.; Chen, J.; Deng, T.; Wang, R.; Jiang, J.; Wang, C. Azo Compounds as a Family of Organic Electrode Materials for Alkali-Ion Batteries. *Proc. Natl. Acad. Sci. U. S. A.* **2018**, *115*, 2004−2009.
(43) Multia, J.; Khayyami, A.; Heiska, J.; Karppinen, M. Low-Pressure Thermogravimetric Analysis for Finding Sublimation Temperatures for Organic Precursors in Atomic/Molecular Layer Deposition. *J. Vac. Sci. Technol., A* **2020**, *38*, No. 052406.
(44) Klepper, K. B.; Nilsen, O.; Hansen, P.-A.; Fjellvåg, H. Atomic Layer Deposition of Organic−Inorganic Hybrid Materials Based on Saturated Linear Carboxylic Acids. *Dalt. Trans.* **2011**, *40*, 4636−4646.
(45) Lee, B. H.; Yoon, B.; Abdulagatov, A. I.; Hall, R. A.; George, S. M. Growth and Properties of Hybrid Organic-Inorganic Metalcone Films Using Molecular Layer Deposition Techniques. *Adv. Funct. Mater.* **2013**, *23*, 532−546.
(46) Adamczyk, N. M.; Dameron, A. A.; George, S. M. Molecular Layer Deposition of Poly(p-Phenylene Terephthalamide) Films Using Terephthaloyl Chloride and p-Phenylenediamine. *Langmuir* **2008**, *24*, 2081−2089.
(47) Kaduk, J. a. Terephthalate Salts: Salts of Monopositive Cations. *Acta Crystallogr., Sect. B: Struct. Sci.* **2000**, *56*, 474−485.
(48) Klepper, K. B.; Nilsen, O.; Francis, S.; Fjellvåg, H. Guidance of Growth Mode and Structural Character in Organic−Inorganic Hybrid Materials − a Comparative Study. *Dalt. Trans.* **2014**, *43*, 3492−3500.
(49) Deacon, G. Relationships between the Carbon-Oxygen Stretching Frequencies of Carboxylato Complexes and the Type of Carboxylate Coordination. *Coord. Chem. Rev.* **1980**, *33*, 227−250.
(50) Kavitha, E.; Sundaraganesan, N.; Sebastian, S.; Kurt, M. Molecular Structure, Anharmonic Vibrational Frequencies and NBO Analysis of Naphthalene Acetic Acid by Density Functional Theory Calculations. *Spectrochim. Acta, Part A* **2010**, *77*, 612−619.
(51) Sourisseau, C.; Maraval, P. Optical and Resonance Raman Scattering Study of Two 'Bisazo' Pigments Derived from Substituted Benzene-2′-Azonaphthols. *J. Raman Spectrosc.* **1994**, *25*, 477−488.
(52) Barnes, A. J.; Majid, M. A.; Stuckey, M. A.; Gregory, P.; Stead, C. V. The Resonance Raman Spectra of Orange II and Para Red: Molecular Structure and Vibrational Assignment. *Spectrochim. Acta Part A Mol. Spectrosc.* **1985**, *41*, 629−635.
(53) Fédèle, L.; Sauvage, F.; Bois, J.; Tarascon, J.-M. M.; Bécuwe, M. Lithium Insertion/De-Insertion Properties of π-Extended Naphthyl-Based Dicarboxylate Electrode Synthesized by Freeze-Drying. *J. Electrochem. Soc.* **2014**, *161*, A46−A52.
(54) Li, C.; Xue, J.; Ma, J.; Li, J. Conjugated Dicarboxylate with Extended Naphthyl Skeleton as an Advanced Organic Anode for Potassium-Ion Battery. *J. Electrochem. Soc.* **2019**, *166*, A5221−A5225.

https://dx.doi.org/10.1021/acsami.0c11822
ACS Appl. Mater. Interfaces 2020, 12, 41557−41566

(55) Sakaushi, K.; Hosono, E.; Nickerl, G.; Gemming, T.; Zhou, H.; Kaskel, S.; Eckert, J. Aromatic Porous-Honeycomb Electrodes for a Sodium-Organic Energy Storage Device. *Nat. Commun.* **2013**, *4*, 1485.
(56) Muench, S.; Wild, A.; Friebe, C.; Häupler, B.; Janoschka, T.; Schubert, U. S. Polymer-Based Organic Batteries. *Chem. Rev.* **2016**, *116*, 9438−9484.
(57) Gu, T.; Zhou, M.; Huang, B.; Cao, S.; Wang, J.; Tang, Y.; Wang, K.; Cheng, S.; Jiang, K. Advanced Li-Organic Batteries with Super-High Capacity and Long Cycle Life via Multiple Redox Reactions. *Chem. Eng. J.* **2019**, *373*, 501−507.
(58) Lee, H. H.; Park, Y.; Shin, K. H.; Lee, K. T.; Hong, S. Y. Abnormal Excess Capacity of Conjugated Dicarboxylates in Lithium-Ion Batteries. *ACS Appl. Mater. Interfaces* **2014**, *6*, 19118−19126.
(59) Heiska, J.; Nisula, M.; Rautama, E.-L.; Karttunen, A. J.; Karppinen, M. Atomic/Molecular Layer Deposition and Electrochemical Performance of Dilithium 2-Aminoterephthalate. *Dalt. Trans.* **2020**, *49*, 1591−1599.
(60) Zhao, Q.; Zhu, Z.; Chen, J. Molecular Engineering with Organic Carbonyl Electrode Materials for Advanced Stationary and Redox Flow Rechargeable Batteries. *Adv. Mater.* **2017**, *29*, 1607007.
(61) Renault, S.; Oltean, V. A.; Araujo, C. M.; Grigoriev, A.; Edström, K.; Brandell, D. Superlithiation of Organic Electrode Materials: The Case of Dilithium Benzenedipropiolate. *Chem. Mater.* **2016**, *28*, 1920−1926.
(62) Han, X.; Qing, G.; Sun, J.; Sun, T. How Many Lithium Ions Can Be Inserted onto Fused C 6 Aromatic Ring Systems? *Angew. Chem., Int. Ed.* **2012**, *51*, 5147−5151.
(63) Hay, M. B.; Myneni, S. C. B. Structural Environments of Carboxyl Groups in Natural Organic Molecules from Terrestrial Systems. Part 1: Infrared Spectroscopy. *Geochim. Cosmochim. Acta* **2007**, *71*, 3518−3532.
(64) Wang, L.; Mou, C.; Wu, B.; Xue, J.; Li, J. Alkaline Earth Metal Terephthalates $MC_8H_4O_4$ (M = Ca, Sr, Ba) as Anodes for Lithium Ion Batteries. *Electrochim. Acta* **2016**, *196*, 118−124.
(65) Medabalmi, V.; Ramanujam, K. Introduction of Carbonyl Groups: An Approach to Enhance Electrochemical Performance of Conjugated Dicarboxylate for Li-Ion Batteries. *J. Electrochem. Soc.* **2017**, *164*, A1720−A1725.
(66) Walker, W.; Grugeon, S.; Vezin, H.; Laruelle, S.; Armand, M.; Wudl, F.; Tarascon, J.-M. Electrochemical Characterization of Lithium 4,4′-Tolane-Dicarboxylate for Use as a Negative Electrode in Li-Ion Batteries. *J. Mater. Chem.* **2011**, *21*, 1615−1620.
(67) Zhao, Y.; Zheng, K.; Sun, X. Addressing Interfacial Issues in Liquid-Based and Solid-State Batteries by Atomic and Molecular Layer Deposition. *Joule* **2018**, *2*, 2583−2604.
(68) Deng, S.; Li, X.; Ren, Z.; Li, W.; Luo, J.; Liang, J.; Liang, J.; Banis, M. N.; Li, M.; Zhao, Y.; Li, X.; Wang, C.; Sun, Y.; Sun, Q.; Li, R.; Hu, Y.; Huang, H.; Zhang, L.; Lu, S.; Luo, J.; Sun, X. Dual-Functional Interfaces for Highly Stable Ni-Rich Layered Cathodes in Sulfide All-Solid-State Batteries. *Energy Storage Mater.* **2020**, *27*, 117−123.
(69) Wang, H.; Liu, Y.; Li, Y.; Cui, Y. Lithium Metal Anode Materials Design: Interphase and Host. *Electrochem. Energy Rev.* **2019**, *2*, 509−517.
(70) Momma, K.; Izumi, F. VESTA 3 for Three-Dimensional Visualization of Crystal, Volumetric and Morphology Data. *J. Appl. Crystallogr.* **2011**, *44*, 1272−1276.

https://dx.doi.org/10.1021/acsami.0c11822
ACS Appl. Mater. Interfaces 2020, 12, 41557−41566